Operation of a Six-phase Induction Machine using Series-connected Machine-side Converters

Hang Seng Che, Emil Levi, *Fellow, IEEE*, Martin Jones, Mario J. Duran, Wooi Ping Hew, Nasrudin Abd. Rahim, *Senior Member, IEEE*

***Abstract*– This paper discusses the operation of a multiphase system, aimed at both variable-speed drive and generating (e.g. wind energy) applications, using back-to-back converter structure with dual three-phase machine-side converters. In the studied topology, an asymmetrical six-phase induction machine is controlled using two three-phase two-level voltage source converters (VSCs) connected in series to form a cascaded dc-link. The suggested configuration is analysed and a method for dc-link midpoint voltage balancing is developed. Voltage balancing is based on the use of additional degrees of freedom that exist in multiphase machines and represents an entirely new utilisation of these degrees. Validity of the topology and its control is verified by simulation and experimental results on a laboratory-scale prototype, thus proving that it is possible to achieve satisfactory dc-link voltage control under various operating scenarios.**

I. Introduction

The standard solution for medium voltage high-power variable-speed drives is nowadays based on the back-to-back converter topology. The converters are typically three-level and a three-phase machine is used [1,2]. The same configuration is also applicable in conjunction with wind energy generators, based on fully-rated converters. Compared to conventional three-phase machines, multiphase machines are credited with having lower torque ripple, better fault-tolerance and lower per-phase power rating requirement [3]. These desirable features make multiphase machines a promising candidate for high power and/or high reliability applications. The majority of the literature deals with multiphase motor drives. However, studies of multiphase generators including five-phase [4], six-phase [5-10], nine-phase [11], twelve-phase [12-14] and eighteen-phase [15] systems have also been reported. Most of these works have been related to wind energy systems, because the increasing power rating (currently up to 10 MW) and reliability requirements (especially in offshore farms) match the advantageous features of multiphase machinery.

Multiphase variable-speed drive systems with back-to back converter configuration utilise typically a multiphase two-level or three-level voltage source converter at the machine side [3]. Multiphase generator studies have concentrated on the use of standard *n*-phase voltage source converters (VSCs) or diode rectifiers, depending on the machine type, with *n* converter legs connected in parallel to the dc-link. Such a topology where two parallel three-phase VSCs drive a six-phase wind energy system is shown in Fig. 1(a). This is at the same time the typical configuration of an asymmetrical six-phase machine when used in a variable-speed drive system.

In [5], a unique converter topology was introduced for an asymmetrical six-phase generator (permanent magnet synchronous machine was considered). The topology uses two three-phase machine-side converters which are connected in series to form a cascaded dc-link. A three-level neutral point clamped (NPC) converter was used as the grid-side converter in a back-to-back manner, with a connection to the dc-link midpoint, as shown in Fig. 1(b). In this configuration, the machine-side converters can provide additional control to the dc-link midpoint voltage balancing and improve the transient performance [16]. A similar concept, using twelve-

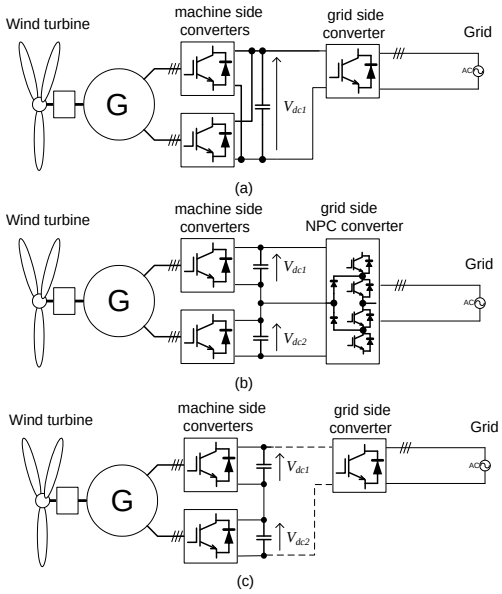

Fig. 1. Six-phase generation system with (a) parallel machine-side converters, (b) series machine-side converters with dc-link midpoint connection and (c) series machine-side converter without dc-link midpoint connection.

Manuscript received August 24, 2012; revised November 07, 2012 and January 18, 2013. Accepted January 23, 2013.

H.S. Che is with the University of Malaya, UMPEDAC Research Centre, Kuala Lumpur, Malaysia and with Liverpool John Moores University, School of Engineering, Technology and Maritime Operations, Liverpool L3 3AF, U.K. (e-mail: h.s.che@2011.ljmu.ac.uk).

E. Levi and M. Jones are with the School of Engineering, Technology and Maritime Operations, Liverpool John Moores University, Liverpool L3 3AF, U.K. (e-mails: e.levi@ljmu.ac.uk and m.jones2@ljmu.ac.uk).

M.J. Duran is with the Department of Electrical Engineering, University of Malaga, 29071 Malaga, Spain (e-mail: mjduran@uma.es).

N.A. Rahim and W.P. Hew are with the UMPEDAC Research Centre, Wisma R&D, University of Malaya, 59990 Kuala Lumpur, Malaysia (e-mails: nasrudin@um.edu.my and wphew@um.edu.my).

phase permanent magnet machine and Vienna rectifiers, is presented in [14]. The topology of Fig. 1(b) is equally applicable to the variable-speed drives as well and can be used in conjunction with both permanent magnet synchronous and induction machines. The series-connected machine-side topology means that the individual dc-link voltages (V_{dc1} and V_{dc2} in Fig. 1(b)) of the six-phase system need only be equal to 50% of the total required dc voltage, achieving a higher total dc-link voltage (V_{dc1}+V_{dc2}) for the same voltage rating of the converters. The *dv/dt* of the common-mode voltage (CMV), which is known to be a main cause of leakage currents in high power applications, is therefore halved as well. The total number of the semiconductor switches of the machine–side converter for a six-phase machine with two-level VSCs is equal to what is required for a three-level three-phase VSC. The elevated dc-link voltage in this series-connected topology reduces the current rating and the cable size for the given power, hence giving a potential overall capital cost reduction.

Although the voltage of the converters is halved in the series connection, it should be noted that the voltage stress within the machine can still reach a value up to the total dc-link voltage (V_{dc}). Nevertheless, since not the whole machine is under this maximum voltage stress, the overall insulation requirement is expected to be lower than that of a higher-voltage machine designed with phase voltage rating based on the full V_{dc} voltage. As a matter of fact, part of the voltage stress can be reduced via proper choice of the PWM technique, as discussed later in Section III.

Although the topology of [5] is potentially interesting, the three-wire connection shown in Fig. 1(b) can be uneconomical if the dc-link is long and the grid-side converter is located far apart. While this may or may not be relevant for variable-speed drive applications, it would be relevant in offshore wind farms with a dc-offshore grid and high voltage direct current (HVDC) transmission to the onshore grid-side converter [17]. Offshore wind farms are currently promoted by some country policies [18] and manufacturers (e.g. RePower [19]) due to the better wind resources and absence of the visual impact. Newly designed offshore wind farms require higher powers and better reliability, which makes them suitable for the utilisation of multiphase generators. If the wind farm distance to the shore is above a certain break-even distance (typically around 70 kilometres [19]), the use of HVDC transmission becomes more favourable and the three-wire topology of Fig. 1(b) is not adequate. For this reason, the topology in [5] has been modified in [20] to eliminate the need for the dc-link midpoint connection to the grid side, as shown in Fig. 1(c). This provides a favourable arrangement for remote offshore wind generation with dc-offshore grid.

Since the grid-side converter can no longer control the voltage of the dc-link midpoint, the voltage drifting becomes a problem for this topology unless the dc-link voltages can be controlled from the machine side. Fortunately, the additional degrees of freedom of the six-phase machine allow the voltage balancing using an additional controller [20]. This paper extends the initial discussion of the suggested topology and its control in [20] (Fig. 1(c)) and provides simulation and experimental verification of the voltage balancing controller performance. It should be noted that the additional degrees of freedom of a multiphase machine have been used in the past for various specific aims (e.g., torque enhancement with low-order stator current harmonic injection, development of fault-tolerant control algorithms for post-fault operation, independent control of a multitude of series-connected multiphase machines using a single voltage source converter [3]). However, there is no evidence that the capacitor voltage balancing has ever been attempted before by utilising these additional degrees of freedom.

The concept of cascading converters to achieve elevated dc link voltage is of course not new, and it has been reported in several works [8], [14], [21-26]. However, such solutions usually require specially designed machines or customised converters. When diode-based rectifiers are used, the applicability is restricted to synchronous generators. The topology discussed here uses standard three-phase VSCs which provide advantages in terms of economy and technology maturity. Moreover, the use of VSCs allows the topology to be used also with induction machines, in both motoring and generating mode.

The paper is organised as follows: Section II presents an overall description of the system, including the topology, induction machine model and control structure. Section III analyses the merits and demerits of the topology and the dc-link voltage drifting issue. Detailed derivation of the dc-link voltage controller is given in Section IV. The theoretical development is supported using simulation and experimental results, provided in Section V. Finally, concluding remarks are given in Section VI.

II. System Description

A. System Topology

In this study, the machine is an asymmetrical six-phase (two three-phase windings spatially shifted by 30º) squirrel-cage induction machine with two isolated neutral points, driven by two three-phase two-level VSCs which are connected in series to form a cascaded dc-link. Since the focus of the discussion is on the machine-side converters, a three-phase two-level VSC is considered as the grid-side converter in this study, for the sake of simplicity. However, it should be emphasised that the grid-side converter is not restricted to the two-level VSC and, as already noted, more advanced converters, such as multilevel neutral-point clamped (NPC) converters, can also be used.

B. Induction Machine Model

Using the vector space decomposition (VSD) technique, the machine model can be decoupled into three orthogonal subspaces, denoted as α-β, *x*-*y* and zero-sequence subspaces. For machines with distributed windings, only α-β components contribute to the useful electromechanical energy conversion, while *x*-*y* and zero-sequence components only produce losses. These *x*-*y* current components represent the additional degrees of freedom, referred to previously. Power invariant decoupling transformation is used to convert the phase variables of the stator ($a1$, $b1$, $c1$, $a2$, $b2$ and $c2$) and rotor

windings into α-β and x-y variables [3]:

$$[T]=\frac{1}{\sqrt{3}}\begin{array}{c}\\ \alpha\\ \beta\\ x\\ y\end{array}\begin{bmatrix} 1 & -\frac{1}{2} & -\frac{1}{2} & \frac{\sqrt{3}}{2} & -\frac{\sqrt{3}}{2} & 0 \\ 0 & \frac{\sqrt{3}}{2} & -\frac{\sqrt{3}}{2} & \frac{1}{2} & \frac{1}{2} & -1 \\ 1 & -\frac{1}{2} & -\frac{1}{2} & -\frac{\sqrt{3}}{2} & \frac{\sqrt{3}}{2} & 0 \\ 0 & -\frac{\sqrt{3}}{2} & \frac{\sqrt{3}}{2} & \frac{1}{2} & \frac{1}{2} & -1 \end{bmatrix} \quad (1)$$

Transformation (1) is the Clarke's matrix for an asymmetrical six-phase system. Zero-sequence components are omitted from the consideration (and are therefore not included in (1)) since the machine has two isolated neutral points. Two pairs of real variables that result after application of (1) onto phase quantities (α–β and x–y) can be combined into corresponding space vectors [3].

A rotational transformation is applied next to transform the α-β variables into a synchronously rotating reference frame (d-q), suitable for vector control [3]:

$$[D]=\begin{array}{c}\\ d\\ q\\ x\\ y\end{array}\begin{bmatrix} \cos\theta_s & \sin\theta_s & & \\ -\sin\theta_s & \cos\theta_s & & \\ & & 1 & \\ & & & 1 \end{bmatrix} \quad (2)$$

The transformation of d-q variables in (2) is identical as in the case of a three-phase system [3]. The second pair of variables (x-y) is not rotationally transformed since the equations for these variables do not contain stator-to-rotor coupling (x-y quantities do not contribute to the electromagnetic torque and hence electromechanical energy conversion). In (2) θ_s is the angle of the rotational transformation for stator. Assuming that the electrical angular speed of the machine is ω_r and the reference frame is rotating at an arbitrary speed ω (so that $\theta_s = \int \omega dt$), the model of the induction machine can be described using the following voltage and flux equations in the d-q plane (indices s and r indicate stator and rotor quantities, respectively; motoring convention for the positive stator current flow is used):

$$\begin{aligned} v_{ds} &= R_s i_{ds} + d\psi_{ds}/dt - \omega\psi_{qs} \\ v_{qs} &= R_s i_{qs} + d\psi_{qs}/dt + \omega\psi_{ds} \\ 0 &= R_r i_{dr} + d\psi_{dr}/dt - (\omega-\omega_r)\psi_{qr} \\ 0 &= R_r i_{qr} + d\psi_{qr}/dt + (\omega-\omega_r)\psi_{dr} \end{aligned} \quad (3)$$

$$\begin{aligned} \psi_{ds} &= (L_{ls}+L_m)i_{ds} + L_m i_{dr} \\ \psi_{qs} &= (L_{ls}+L_m)i_{qs} + L_m i_{qr} \\ \psi_{dr} &= (L_{lr}+L_m)i_{dr} + L_m i_{ds} \\ \psi_{qr} &= (L_{lr}+L_m)i_{qr} + L_m i_{qs} \end{aligned} \quad (4)$$

R_s and R_r are stator and rotor resistances, while L_{ls}, L_{lr} and L_m are stator and rotor leakage and magnetising inductances, respectively. Additional stator equations, which describe the machine in the x-y plane, are:

$$\begin{aligned} v_{xs} &= R_s i_{xs} + d\psi_{xs}/dt \\ v_{ys} &= R_s i_{ys} + d\psi_{ys}/dt \end{aligned} \quad (5)$$

$$\begin{aligned} \psi_{xs} &= L_{ls} i_{xs} \\ \psi_{ys} &= L_{ls} i_{ys} \end{aligned} \quad (6)$$

For a machine with p pole pairs, the electromagnetic torque solely depends on the d-q components and is given with:

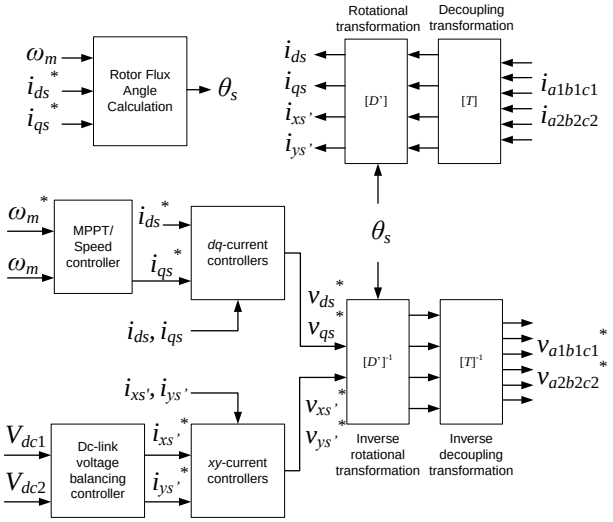

Fig. 2. General structure of the machine-side controllers.

$$T_e = pL_m\left[i_{dr}i_{qs} - i_{ds}i_{qr}\right] \quad (7)$$

Finally, the equation of rotor motion is:

$$T_e - T_m = J\frac{d\omega_m}{dt} \quad (8)$$

where ω_m is the rotor mechanical speed, J is the inertia, and T_m is the mechanical (prime mover or load) torque.

C.Control Structure

Based on the VSD model, the six-phase induction machine is controlled using indirect rotor flux oriented control (IRFOC). Rotor flux angle, required for the rotational transformation (2), is calculated on the basis of the standard indirect orientation principles, using slip frequency ω_{sl}^*.

$$\theta_s = \int\left(p\omega_m + \omega_{sl}^*\right)dt \quad (9)$$

$$\omega_{sl}^* = \frac{1}{T_r}\frac{i_{qs}^*}{i_{ds}^*} \quad (10)$$

Due to the additional degrees of freedom, instead of using just two PI controllers for the d-q current control, two extra current controllers are required for the x-y current control. The schematic of the machine-side current control is shown in Fig. 2. There are various control schemes that can be used for the x-y current control in multiphase machines [27], [28]. Here, an anti-synchronous reference frame is used for the x-y PI current controllers since it allows an easy implementation of the dc-link voltage balancing control. Superscript $'$ is added to the rotational transformation matrix [D] and x-y currents in Fig. 2 to differentiate them from those based on equation (2). Detailed explanation of the dc-link voltage balancing controller using PI current controllers in anti-synchronous reference frame is postponed for Section IV. The d-axis current reference (i_{ds}^*) is set at a constant value to provide rated rotor flux and the q-axis current reference (i_{qs}^*) is provided by either a maximum power point tracking (MPPT) controller, based on the optimal torque control method [19] when operating as a generator, or by a PI speed controller when operating in motoring mode.

Since the dc-link practically decouples the grid-side converter from the machine-side converters and the total dc-link voltage is controlled by the grid side converter, the grid-side converter can be conveniently represented by a controllable current source in the simulation (and a constant voltage supply in the experiment). The current source (voltage supply) only operates to maintain the overall dc-link voltage at a constant level, and will therefore not be discussed in detail here.

III. Analysis of Series-Converter Topology

A. Merits and Demerits of the Topology

The topology of Fig. 1(c) combines an asymmetrical six-phase induction machine with cascaded machine-side converters. The series connection of the converters elevates the dc-link voltage, thus reducing the current rating and losses for the given dc-link voltage level. In generating mode, the higher generating voltage also eases the step-up voltage process to the transmission voltage level.

The cascaded dc-links also allow supplying each set of three-phase windings with halved dc-link voltage (Fig. 1(c)). This lowers dc-link voltage ($V_{dc1} = V_{dc1} = V_{dc}/2$) and allows the use of switching devices with lower voltage ratings. The reduced dc-link voltage also halves the *dv/dt* of the common-mode voltage (CMV) for each winding, which now has steps of $V_{dc1}/3 = V_{dc}/6$, compared to the value of $V_{dc}/3$ in three-phase machines, for the given V_{dc} value.

As with other transformerless converter topologies [8], [23], one major challenge for this topology is the machine's insulation requirement. In this topology, the upper and lower dc-link voltages (referenced to the dc-link midpoint) are $V_{dc}/2$ and 0 for VSC1 and 0 and $-V_{dc}/2$ for VSC2. Hence, while the voltage within each set of three-phase windings is restricted to $V_{dc}/2$, the voltage stress between the two sets of windings can reach V_{dc}.

Nevertheless, not all parts of the machine are subjected to this maximum voltage stress. In particular, the voltage difference between neutral points of the two set of windings actually varies depending on the switching state, as summarised in Table I. Switching states are expressed in decimal form of the six digit binary number $S_{a1}\ S_{b1}\ S_{c1}\ S_{a2}\ S_{b2}\ S_{c2}$, where S_i denotes the switching condition of converter leg for phase *i*, with 0 indicating lower switch turned on and 1 indicating upper switch turned on. Redundant states are given in bold.

As shown in Table I, the neutral-to-neutral voltage varies from 0 to as high as V_{dc}, depending on the switching state. By selecting a suitable pulse-width modulation (PWM) method, the neutral-to-neutral voltage can be limited to lower values. PWM methods that use the switching state 56 (111000), as does the 24-sector SVPWM [29], should be avoided, as they exert large voltage stress (V_{dc}) on the windings. PWM using double zero-sequence injection [30] is used throughout this paper, in both simulations and experiments, since this method does not apply switching state 56 (111000). As a matter of fact, only switching states that produce 0.333, 0.5 and 0.667 V_{dc} are used in this PWM method, as it will be seen later in the experimental results. The presence of redundant states suggests the possibility of further reducing the voltage stress using special space vector PWM techniques which restrict selection of certain switching states [31]. This is however beyond the scope of this paper and not discussed further.

TABLE I. NEUTRAL-TO-NEUTRAL VOLTAGE FOR DIFFERENT SWITCHING STATES.

Neutral-to-neutral voltage (p.u. of V_{dc})	**Switching states**
1.0	**56(111000)**
0.833	**24(011000)**, **40(101000)**, **48(110000)**, **57(111001)**, **58(111010)**, **60(111100)**
0.667	**8(001000)**, **16(010000)**, 25(011001), 26(011010), 28(011100), **32(100000)**, 41(101001), 42(101010), 44(101100), 49(110001), 50(110010), 52(110100), **59(111011)**, **61(111101)**, **62(111110)**
0.500	**0 (000000)**, 9(001001), 10(001010), 12(001100), 17(010001), 18(010010), 20(010100), 27(011011), 29(011101), 30(011110), 33(100001), 34(100010), 36(100100), 43(101011), 45(101101), 46(101110), 51(110011), 53(110101), 54(110110), **63(111111)**
0.333	**1(000001)**, **2(000010)**, **4(000100)**, 11(001011), 13(001101), 14(001110), 19(010011), 21(010101), 22(010110), **31(011111)**, 35(100011), 37(100101), 38(100110), **47(101111)**, **55(110111)**
0.167	**3(000011)**, **5(000101)**, **6(000110)**, **15(001111)**, **23(011111)**, **39(110111)**
0	**7(000111)**

Since not every part of the machine winding requires the insulation to withstand maximum voltage stress of V_{dc}, it is possible to relax the insulation requirements by proper machine design. For instance, slot sharing between conductors from different sets of windings should be avoided. Hence, as noted, even though the insulation requirement is high, it can be comparatively less than in a similar machine designed with phase voltage rating based on full V_{dc} voltage.

B. Dc-Link Voltage Drift

In the considered topology the dc-link midpoint at the machine side is not accessible by the grid-side converter any more, while the total dc-link voltage control is performed by the grid-side converter. There is no guarantee whatsoever that the dc-link voltages (V_{dc1} and V_{dc2} in Fig. 1(c)) will always be balanced. It is thus necessary to control the dc-link voltages at the machine side using the machine-side converters, to avoid dc-link voltage drift. In order to analyse the dc-link voltage balancing issue, the system is simplified by representing each VSC as a controlled current source, as shown in Fig. 3.

By using Kirchhoff's current law for points W and Z, the machine-side converters' currents can be written as:

$$I_{dc1} = -I_{dc3} - I_{cap1} \qquad I_{dc2} = -I_{dc3} - I_{cap2} \tag{11}$$

The currents I_{dc1} and I_{dc2} consist of two components: a common component ($-I_{dc3}$) and a differential component (I_{cap1} and I_{cap2}). At any time instant, the common current component will be drawn from both machine-side converters, while the instantaneous difference between the converters' currents and the common current will be supplemented by each of the converter's capacitors. Ideally, the two sets of machine windings are identical, so the average converter current should be the same despite the spatial difference. The average capacitor currents should thus also be the same.

The dc-link voltage balancing depends on the active power

balancing between the two converters. The equations for the active power of the machine-side converters are:

$$P_1 = I_{dc1}V_{dc1} \qquad P_2 = I_{dc2}V_{dc2} \tag{12}$$

During steady state, the average converters' currents will be equal. Hence,

$$\frac{P_1}{P_2} = \frac{V_{dc1}}{V_{dc2}} \tag{13}$$

If the grid-side converter provides perfect control, the total dc-link voltage will be maintained at a constant value of V_{dc}. Each individual dc-link voltage is expressed as a sum of its ideal balanced value ($V_{dc}/2$) and a deviation from the ideal value (ΔV_{dc1} and ΔV_{dc2}). Since the sum of two dc-link voltages is equal to V_{dc}, the voltage deviations must be equal but of opposite sign, i.e. $\Delta V_{dc1} = -\Delta V_{dc2}$. Hence the power equation (13) can be written as:

$$\frac{P_1}{P_2} = \frac{(V_{dc}/2) + \Delta V_{dc1}}{(V_{dc}/2) - \Delta V_{dc1}} \tag{14}$$

Rearranging (14), the voltage deviation can be expressed as a function of the active powers:

$$\Delta V_{dc1} = \left(\frac{P_1 - P_2}{P_1 + P_2}\right)\frac{V_{dc}}{2} \tag{15}$$

From (15) it follows that any asymmetry in the system will cause dc-link voltage drifting unless some voltage balancing mechanism is included in the control scheme.

IV. DC-Link Voltage Balancing Control

A. Dc-Link Voltage Balancing Using x-y Currents

Based on the analysis in Section III, it is obvious that additional control needs to be provided by the machine-side converters to ensure the dc-link voltages are always balanced.

This can be achieved using the additional degrees of freedom provided by the *x-y* currents, so that the torque and flux production of the machine remains unaffected. Since the dc-link voltage unbalance is found to be a result of active power imbalance, it is necessary to first identify the relation between the *x-y* currents and the active power difference between the two windings. With the VSD model, the quantities in the two pairs of windings are not related, while the powers of the two three-phase windings now need to be controlled separately. In order to achieve separate power control with the VSD model, it is insightful to at first establish the relationship between *d-q-x-y* components in the VSD model and the d_1-q_1–d_2-q_2 components in the dual *d-q* model [20], which enables separate formulation of winding powers.

To start with, according to the stationary transformation of the dual *d-q* model, the α-β components of the two windings are separately treated as α_1-β_1 and α_2-β_2 currents, which can be given with:

$$\begin{aligned}
i_{\alpha s1} &= \sqrt{\tfrac{2}{3}}\left(i_{a1} - \tfrac{1}{2}i_{b1} - \tfrac{1}{2}i_{c1}\right)\\
i_{\alpha s2} &= \sqrt{\tfrac{2}{3}}\left(\tfrac{\sqrt{3}}{2}i_{a2} - \tfrac{\sqrt{3}}{2}i_{b2}\right)\\
i_{\beta s1} &= \sqrt{\tfrac{2}{3}}\left(\tfrac{\sqrt{3}}{2}i_{b1} - \tfrac{\sqrt{3}}{2}i_{c1}\right)\\
i_{\beta s2} &= \sqrt{\tfrac{2}{3}}\left(\tfrac{1}{2}i_{a2} + \tfrac{1}{2}i_{b2} - i_{c2}\right)
\end{aligned} \tag{16}$$

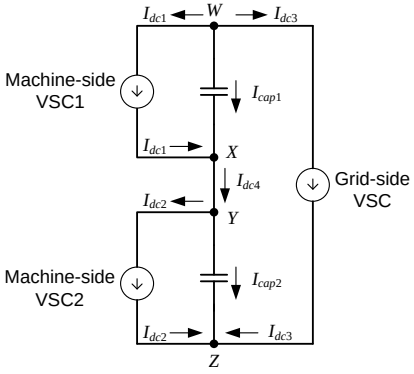

Fig. 3. Simplified circuit diagram for generation system with series-connected dc-links.

Comparison of (16) with (1) shows that the following holds true:

$$\begin{aligned}
i_{\alpha s} &= \sqrt{\tfrac{1}{2}}\left(i_{\alpha s1} + i_{\alpha s2}\right) & i_{\beta s} &= \sqrt{\tfrac{1}{2}}\left(i_{\beta s1} + i_{\beta s2}\right)\\
i_{xs} &= \sqrt{\tfrac{1}{2}}\left(i_{\alpha s1} - i_{\alpha s2}\right) & i_{ys} &= \sqrt{\tfrac{1}{2}}\left(-i_{\beta s1} + i_{\beta s2}\right)
\end{aligned} \tag{17}$$

For control purposes, it is more useful to have the control variables in the *d-q* synchronous reference frame, so that they appear as dc quantities and can hence be easily dealt with using PI controllers. For dual *d-q* model, currents in the synchronously rotating frame are given as:

$$\begin{aligned}
i_{ds1} &= i_{\alpha s1}\cos\theta_s + i_{\beta s1}\sin\theta_s\\
i_{ds2} &= i_{\alpha s2}\cos\theta_s + i_{\beta s2}\sin\theta_s\\
i_{qs1} &= -i_{\alpha s1}\sin\theta_s + i_{\beta s1}\cos\theta_s\\
i_{qs2} &= -i_{\alpha s2}\sin\theta_s + i_{\beta s2}\cos\theta_s
\end{aligned} \tag{18}$$

For the VSD model, using the conventional rotational transformation defined in (2), the following is obtained:

$$\begin{aligned}
i_{ds} &= \sqrt{1/2}\left(i_{ds1} + i_{ds2}\right)\\
i_{qs} &= \sqrt{1/2}\left(i_{qs1} + i_{qs2}\right)\\
i_{xs} &= \sqrt{1/2}\left[\left(i_{ds1} - i_{ds2}\right)\cos\theta_s - \left(i_{qs1} - i_{qs2}\right)\sin\theta_s\right]\\
i_{ys} &= \sqrt{1/2}\left[\left(-i_{ds1} + i_{ds2}\right)\sin\theta_s + \left(-i_{qs1} + i_{qs2}\right)\cos\theta_s\right]
\end{aligned} \tag{19}$$

As can be seen from (19), the resulting *x-y* components are not dc quantities. Hence, an alternative transformation matrix is introduced,

$$[D'] = \begin{matrix} d \\ q \\ x' \\ y' \end{matrix}\begin{bmatrix} \cos\theta_s & \sin\theta_s & & \\ -\sin\theta_s & \cos\theta_s & & \\ & & \cos\theta_s & -\sin\theta_s \\ & & \sin\theta_s & \cos\theta_s \end{bmatrix} \tag{20}$$

which rotates the *x-y* components in the inverse (anti-) synchronous direction. With this alternative rotational transformation, a more suitable form of *x-y* components (denoted as *x'-y'* components) can be obtained:

$$\begin{aligned}
i_{ds} &= \sqrt{1/2}\left(i_{ds1} + i_{ds2}\right)\\
i_{qs} &= \sqrt{1/2}\left(i_{qs1} + i_{qs2}\right)\\
i_{xs'} &= \sqrt{1/2}\left(i_{ds1} - i_{ds2}\right) = \sqrt{1/2}\,\Delta i_{ds}\\
i_{ys'} &= \sqrt{1/2}\left(i_{qs2} - i_{qs1}\right) = -\sqrt{1/2}\,\Delta i_{qs}
\end{aligned} \tag{21}$$

Transformed x'-y' components are now both dc signals and represent the difference between the d-q components of the two windings. Controlling $i_{xs'}$ to be positive will make i_{ds1} greater than i_{ds2}, while positive $i_{ys'}$ makes i_{qs1} smaller than i_{qs2}, and vice versa. Thus, power drawn from the two windings can be controlled by the proper injection of $i_{xs'}$-$i_{ys'}$ currents. Moreover, since d-q components are dc quantities, x'-y' components will also be dc quantities, which allows the use of simple PI controllers. It is also worth noting that, from (21), injecting $i_{xs'}$-$i_{ys'}$ changes the difference between i_{ds1}-i_{qs1} and i_{ds2}-i_{qs2} but does not change the overall flux and torque currents (i_{ds}-i_{qs}). Hence the injection of $i_{xs'}$-$i_{ys'}$ currents will not affect the overall operation of the machine.

During generation, active power is injected into the dc-link and the torque current is negative (assuming positive rotational direction). When ΔV_{dc1} is positive, Δi_{qs} should be positive to reduce power injected by the VSC1, and vice versa. Hence, dc-link voltage balancing controller can be constructed using a PI controller with ΔV_{dc1} as input. Since $i_{ys'}$ and Δi_{qs} have opposite polarity, the output of the PI controller should be inverted (multiplied by -1), as in Fig. 4.

B. Voltage Balancing in Motoring Mode

The derivation of the dc-link voltage balancing controller has been based on the machine operation in the generating mode. The applicability of the same controller structure in the motoring mode is therefore addressed here.

During motoring operation in positive rotational direction, the machine consumes active power from the dc-link and the torque current is positive. When ΔV_{dc1} is positive, positive Δi_{qs} should be imposed so that VSC1 consumes more active power than VSC2, and thus reduces ΔV_{dc1}. Since Δi_{qs} again has the same polarity as ΔV_{dc1}, the same controller structure can be applied during motoring mode as well.

When the machine rotates in the negative direction in motoring mode, the sign of torque current becomes negative. In this case, positive ΔV_{dc1} requires a negative Δi_{qs} for voltage balancing. For proper operation of the dc-link voltage balancing controller, the negative sign in Fig. 4 will have to be replaced by a positive sign. This consideration does not apply in generation, since the rotation of a generator is usually confined to a single direction.

V. Simulation and Experimental Results

In order to verify the dc-link voltage balancing controller operation, experimental tests are conducted on a low-power asymmetrical six-phase induction machine, which was obtained by rewinding a 1.1 kW three-phase machine. The six-phase machine is configured with two isolated neutral points. Each of the two three-phase windings is connected to a custom-made multiphase two-level VSC, configured for three-phase operation. The dc-links of the two VSCs are cascaded in series, and connected to a dc-power supply (Sorensen SGI 600-25) which maintains the overall dc-link voltage at 300 V. A 7.5 kW dc machine is coupled to the six-phase machine and is controlled using ABB DCS800 in torque mode to provide loading of the six-phase machine.

The whole control algorithm for the six-phase machine is implemented using dSpace DS1006 system. Switching frequency of 5 kHz and current sampling frequency of 10 kHz are used. Dead time of 6 μs is integrated in the VSC hardware. Machine phase currents and dc-link voltages are measured (using the LEM sensors embedded in the VSCs) through dSpace DS2004 ADC module and displayed on oscilloscope via the dSpace DS2101 DAC module. Hence the current traces shown later are the filtered current waveforms, without the switching ripples. Overall configuration of the experimental setup is shown in Fig. 5 and the detailed list of machine and control parameters is given in Table II.

Due to the lack of means for grid connection, experimental results apply only to operation in the motoring mode. However, as maintained from the beginning, and as discussed in Section IV-B, the capacitor voltage balancing controller is of the same structure in both motoring and generating applications. All the parameters used for the simulation are identical to those in the experimental setup (except for the machine's inertia and machine's inherent asymmetries, which were obtained via trial and error for simulation purpose).

In what follows the experimental results are shown first, together with Matlab/Simulink simulation results, for the motoring mode of operation. The study is then complemented with simulation results for the generating mode of operation.

A. Experimental Verification in the Motoring Mode

The machine is controlled in motoring mode, using IRFOC with closed-loop speed control. Only d-q current controllers are initially used, without any x-y current control (x-y voltage references are set to zero). Fig. 6 shows the experimental results when the machine operates at 500 rpm without load.

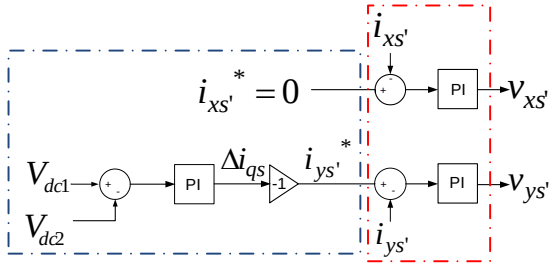

Fig. 4. Structure of the x'-y' current controllers (dotted box on the right) and dc-link voltage balancing controller (dotted box on the left).

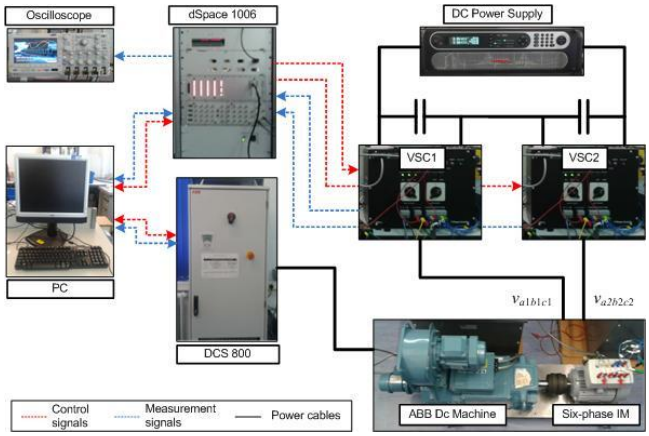

Fig. 5. Experimental setup for the series-converter topology in motoring mode.

TABLE II. EXPERIMENT AND SIMULATION PARAMETERS.

Machine parameters			
R_s = 12.5 Ω	R_r = 6.0 Ω	J = 0.04 kg·m^2	p = 3
L_{ls_dq} = 0.0615 H	L_{lr} = 0.011 H	L_m = 0.590 H	
L_{ls_xy} = 0.0055 H			
Converter Parameters			
$C_1 = C_2$ = 1500 μF	$V_{dc1} = V_{dc2}$ = 150 V		
Controller Parameters			
$f_{switching}$ = 5 kHz	$f_{sampling}$ = 10 kHz		
***d-q* current controllers:**		K_p = 60	K_i = 8000
***x'-y'* current controllers:**		K_p = 50	K_i = 2500
Speed controller:		K_p = 0.02	K_i = 0.02
Dc-link voltage balancing controller:		K_p = 1.0	K_i = 2.0

The dc-link voltages are not equal due to the inherent asymmetries that exist in the converters and the machine. VSC2 is driven into saturation (over-modulation region) by the low dc-link voltage and produces low order harmonics in phase voltages, which cause flow of *x-y* currents. The uncontrolled *x-y* currents produce additional power losses and distort the current waveform, causing the difference in the amplitudes of the currents in windings 1 and 2.

The same operating condition is simulated using Matlab/Simulink and the results are shown in Fig. 7. Inherent asymmetry in the machine/converter is emulated by adding additional resistance R = 2.8 Ω in phases $a1b1c1$ (the value was found via trial and error, so that a close agreement with the experimental findings is obtained). Other than the value of R, all parameters used in the simulation are identical to those used in the actual experiment. The simulated currents closely resemble the experimental results, confirming the accuracy of the simulator.

The same test is repeated for the machine running at 250 rpm, when a larger dc-link voltage drift is observed. Fig. 8 shows the experimental results where the phase currents are more distorted than in the previous case, because VSC2 is in deeper saturation due to the larger dc-link voltage imbalance. Again, simulated results in Fig. 9 show good correlation with the experimental findings.

Figs. 10 and 11 show the experimental and simulation results when anti-synchronous PI *x'-y'* current controllers are activated with *x'-y'* current references set to zero. Since one of the VSCs is now in saturation, the *x'-y'* current controllers, which are designed to operate in the linear modulation region, are unable to fully suppress the *x'-y'* currents and only a slight improvement in terms of the current distortion is obtained. Dc-link voltages remain unbalanced in this case, since the active powers consumed by the two VSCs are still not balanced.

Figs. 12 and 13 show the activation of dc-link voltage balancing controller at t = 1.0 s (t = 5.0 s in Fig. 13), when the machine is running at 500 rpm without load. As predicted by the theoretical considerations, the dc-link voltages converge and stay balanced after the activation of the controller. Figs. 14 and 15 show that the currents for phases $a1$ and $a2$ become much more balanced and are less distorted because the *x-y* currents are now under control and the dc-link voltages are controlled to achieve VSC operation in the linear region. Slight distortion can still be observed due to the dead-time effect of the converter.

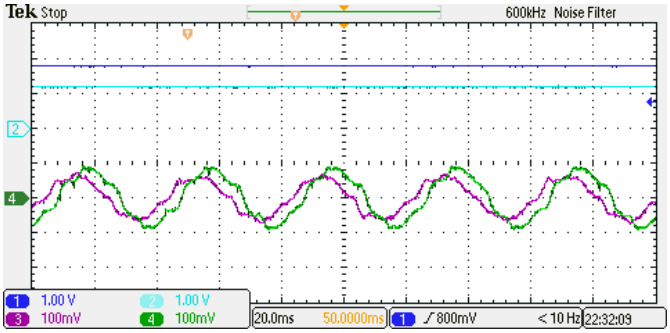

Fig. 6. Experimental results for no-load operation at 500 rpm, with only *d-q* current controllers: Channel 1: V_{dc1} (100V/div), Channel 2: V_{dc2} (100V/div), Channel 3: phase-$a1$ current (1A/div), Channel 4: phase-$a2$ current (1A/div), Horizontal: Time (20ms/div). (Note that markers for Channels 1 and 3 have been overlapped by markers for Channels 2 and 4, respectively).

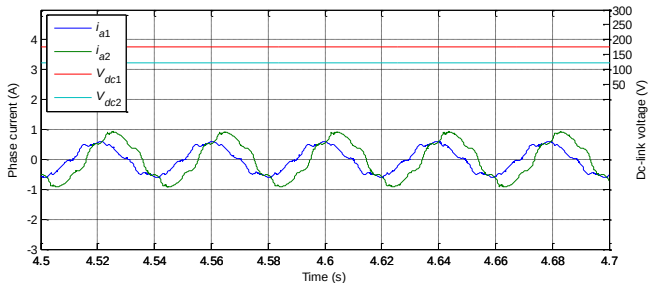

Fig. 7. Simulation results for no-load operation at 500 rpm, with only *d-q* current controllers.

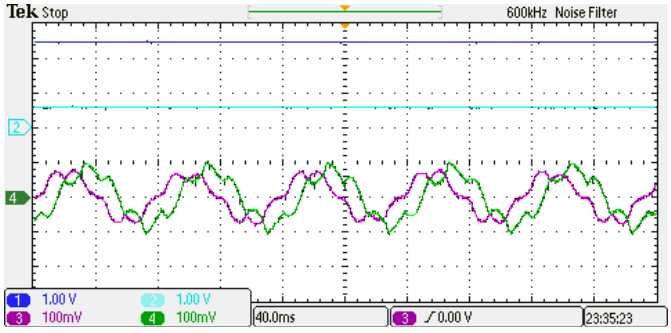

Fig. 8. Experimental results for no-load operation at 250 rpm, with only *d-q* current controllers: Channel 1: V_{dc1} (100V/div), Channel 2: V_{dc2} (100V/div), Channel 3: phase-$a1$ current (1A/div), Channel 4: phase-$a2$ current (1A/div), Horizontal: Time (20ms/div). (Markers for Channels 1 and 3 have been overlapped by markers for Channels 2 and 4, respectively).

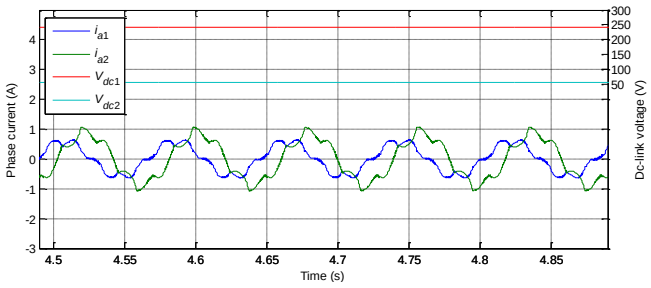

Fig. 9. Simulation results for no-load operation at 250 rpm, with only *d-q* current controllers.

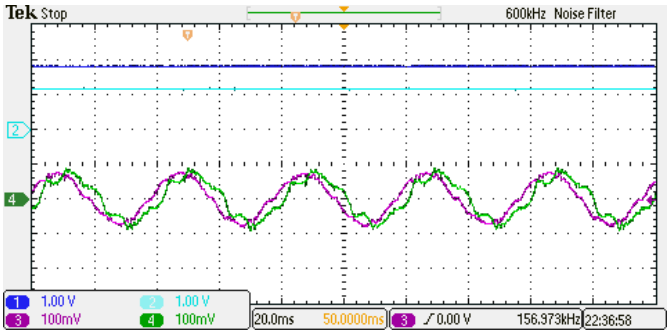

Fig. 10. Experimental results for no-load operation at 500 rpm, with *d*-*q* and *x'*-*y'* current controllers activated: Channel 1: V_{dc1} (100V/div), Channel 2: V_{dc2} (100V/div), Channel 3: phase-*a*1 current (1A/div), Channel 4: phase-*a*2 current (1A/div), Horizontal: Time (20ms/div). (Markers for Channels 1 and 3 have been overlapped by markers for Channels 2 and 4, respectively).

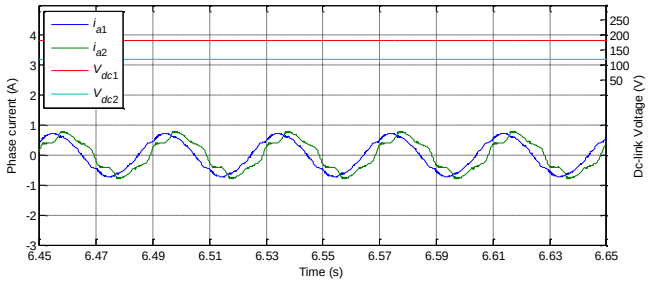

Fig. 11. Simulation results for no-load operation at 500 rpm, with *d*-*q* and *x'*-*y'* current controllers activated.

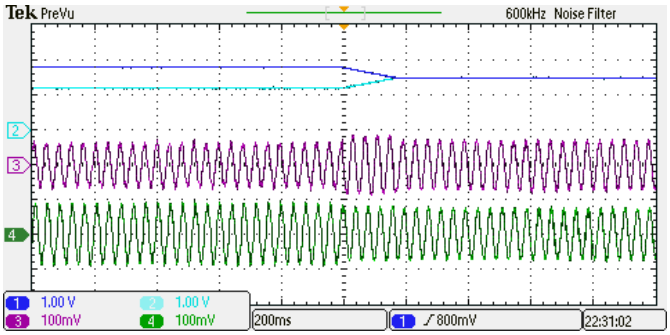

Fig. 12. Experimental results for no-load operation at 500 rpm, showing the activation of the dc-link voltage balancing controller at t = 1.0s: Channel 1: V_{dc1} (100V/div), Channel 2: V_{dc2} (100V/div), Channel 3: phase-*a*1 current (1A/div), Channel 4: phase-*a*2 current (1A/div), Horizontal: Time (200ms/div). (Markers for Channels 1 and 2 are overlapped).

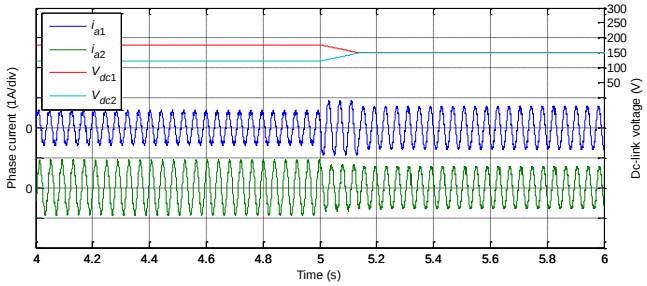

Fig. 13. Simulation results for no-load operation at 500 rpm, showing the activation of the dc-link voltage balancing controller at t = 5.0s.

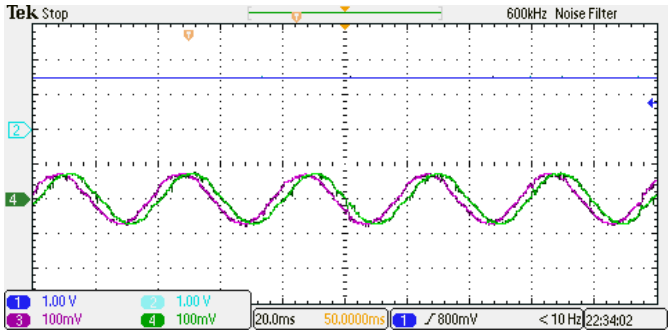

Fig. 14. Experimental results for no-load operation at 500 rpm, with dc-link voltage balancing controller activated: Channel 1: V_{dc1} (100V/div), Channel 2: V_{dc2} (100V/div), Channel 3: phase-*a*1 current (1A/div), Channel 4: phase-*a*2 current (1A/div), Horizontal: Time (20ms/div). (Markers for Channels 1 and 3 have been overlapped by markers for Channels 2 and 4, respectively).

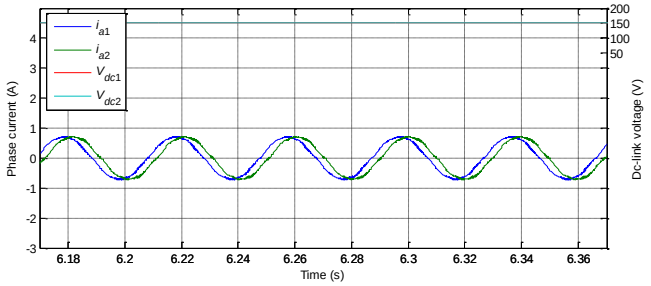

Fig. 15. Simulation results for no-load operation at 500 rpm, with dc-link voltage balancing controller activated (V_{dc1} and V_{dc2} are overlapped).

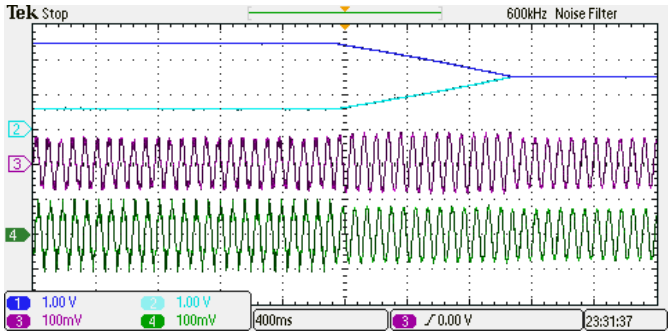

Fig. 16. Experimental results for no-load operation at 250 rpm, showing the activation of dc-link voltage balancing controller at t = 1.0s: Channel 1: V_{dc1} (100V/div), Channel 2: V_{dc2} (100V/div), Channel 3: phase-*a*1 current (1A/div), Channel 4: phase-*a*2 current (1A/div), Horizontal: Time (400ms/div). (Markers for Channels 1 and 2 are overlapped).

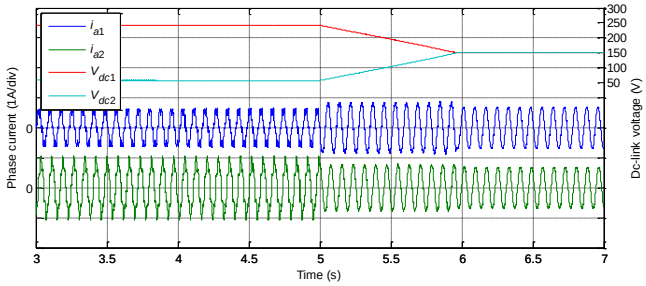

Fig. 17. Simulation results for no-load operation at 250 rpm, showing the activation of dc-link voltage balancing controller at t = 5.0s.

The same procedure is repeated for operation at 250 rpm without load, Figs. 16 and 17. A slower convergence is observed, since the same controller gains and limits are used, while the dc-link voltage difference is now larger.

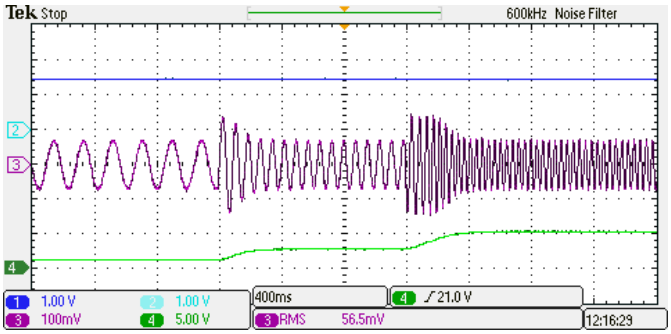

Fig. 18. Experimental results for speed variation from 100rpm to 250rpm to 500rpm under no-load conditions with dc-link voltage balancing controller activated: Channel 1: V_{dc1} (100V/div), Channel 2: V_{dc2} (100V/div), Channel 3: phase-a1 current (1A/div), Channel 4: speed (500rpm/div), Horizontal: Time (400ms/div). (Markers for Channels 1 and 2 are overlapped).

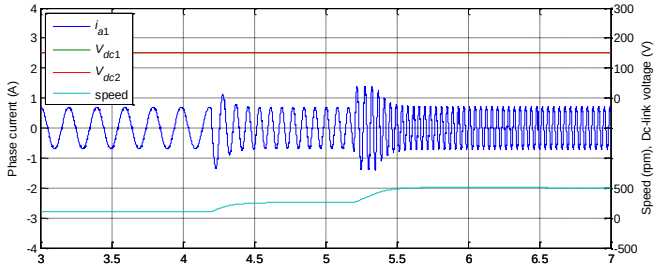

Fig. 19. Simulation results for speed variation from 100 rpm to 250 rpm to 500 rpm (V_{dc1} and V_{dc2} are overlapped).

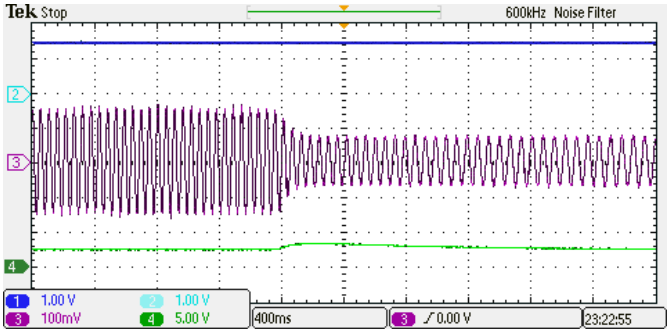

Fig. 20. Experimental results for machine unloading at 250 rpm, with dc-link voltage balancing controller activated: Channel 1: V_{dc1} (100V/div), Channel 2: V_{dc2} (100V/div), Channel 3: phase-a1 current (1A/div), Channel 4: speed (500rpm/div), Horizontal: Time (400ms/div). (Markers for Channels 1 and 2 are overlapped).

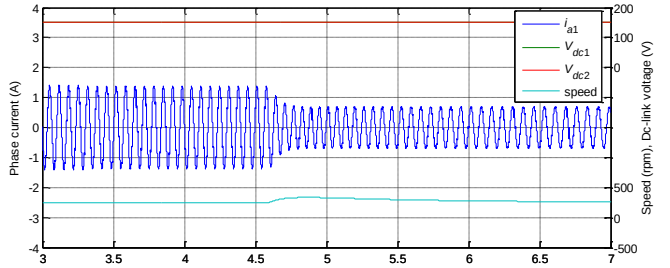

Fig. 21. Simulation results for machine unloading at 250 rpm, with dc-link voltage balancing controller activated (V_{dc1} and V_{dc2} are overlapped).

Next, the performance of the dc-link voltage balancing controller is evaluated with the machine in variable-speed operation. Fig. 18 shows the performance of the dc-link voltage balancing controller when the speed reference increases from 100 rpm to 250 rpm at t = 1.2 s, and then to 500 rpm at t = 2.2 s (t = 4.2 s and t = 5.2 s in the corresponding simulation study in Fig. 19). It is evident that the dc-link voltages are kept at equal values during the whole transient operation.

Performance of the system under sudden load torque variation is also evaluated in Figs. 20 and 21. A torque command is first given to the DCS800, such that the dc-machine provides a load torque to the six-phase machine. Using IRFOC, the six-phase machine is able to maintain the speed at 250 rpm. At t = 1.6 s (t = 4.6 s in Fig. 21), the load torque is removed by reducing the torque command to zero. A speed overshoot is observed together with the current amplitude reduction, as a result of the load torque variation. Nevertheless, the dc-link voltages are kept at equal values throughout this process, showing that the dc-link voltage balancing controller is unaffected by the sudden load torque variation.

Based on (15), it is obvious that dc-link unbalance is a result of power unbalance between the two windings. Fig. 22 shows the comparison of active power supplied to VSC1 and VSC2 before and after the activation of dc-link voltage balancing controller. Results show that the power consumed by each VSC (and hence each winding of the machine) is highly unbalanced before compensation. The compensation restores power balance between the two VSCs. This is accompanied by a slight reduction of total power, which is due to the reduction of loss producing harmonics associated with the saturation of one of the VSCs under unbalanced capacitor voltage. The imbalance in powers, apart from causing unbalanced capacitor voltages, may also require derating of the machine to avoid overloading of one of the windings/converters.

It is worth noting that the unbalance is in this case caused by inherent asymmetries in the machine windings/converters, manifested in the form of small differences in the per-phase resistances. As the load increases, the difference in RI^2 power losses in these resistances becomes marginal; hence power unbalance decreases with increasing load torque.

B. Experimental Results – Operation at Lower Switching Frequency

The experimental results given so far were obtained for 5 kHz switching frequency. Since the topology is aimed at high power applications, experimental results for the operation of the system with a lower switching frequency of 1 kHz are presented next. Operating conditions are the same as for 5 kHz switching frequency, except that the PI controller gains

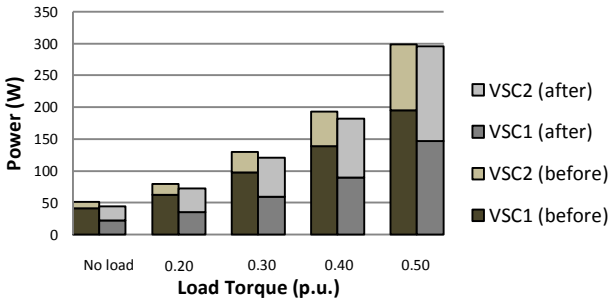

Fig. 22. Comparison of active powers, consumed by each VSC, before (left bars) and after (right bars) activation of the dc-link voltage balancing controller, when the machine operates at 250 rpm with different load torque.

have been reduced to ensure stable operation. Fig. 23 shows the activation of the dc-link voltage balancing controller and Fig. 24 shows the operation of the system under varying speed. While the dynamics of the system differ slightly, the results show that the dc-link voltage controller can still balance the dc-link voltage despite the reduction in the switching frequency.

C.Experimental Results – CMV and Neutral-to-neutral Voltage

This sub-section shows the experimental results for common-mode voltage and neutral-to-neutral voltage in the series-converter topology. The results are obtained for the motoring mode without load, with dc-link voltage balancing controller activated. Overall dc-link voltage is 300 V. Fig. 25 shows the common-mode voltage for winding 1. This voltage is measured as the neutral point voltage of winding 1 with respect to the dc-link mid-point. Zoomed-in view of the voltage waveform shows that the CMV changes in steps of 50V (V_{dc}/6), which agrees with discussion in Section III.

Fig. 26 shows the neutral-to-neutral voltage of the machine under the same operating condition. It is observed that the neutral-to-neutral voltage is around 0.333, 0.5 and 0.667 V_{dc}, since the PWM method used does not utilise states that give neutral-to-neutral voltage of 0, 0.166, 0.833 and 1.0 V_{dc} (as stated in Section III). The *dv/dt* is also reduced since the steps are V_{dc}/6.

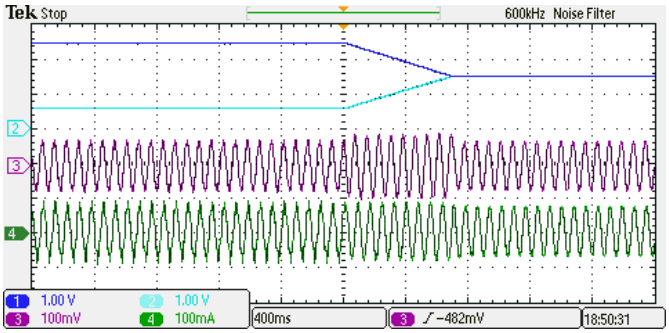

Fig. 23. Experimental results for no-load operation at 250 rpm showing the activation of dc-link voltage balancing controller at t = 1.0s (switching frequency = 1 kHz): Channel 1: V_{dc1} (100V/div), Channel 2: V_{dc2} (100V/div), Channel 3: phase-*a*1 current (1A/div), Channel 4: phase-*a*2 current (1A/div), Horizontal: Time (400ms/div). (Markers for Channels 1 and 2 are overlapped).

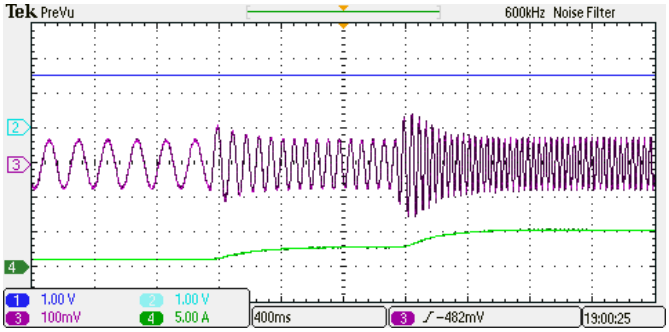

Fig. 24. Experimental results for speed variation from 100rpm to 250rpm to 500rpm under no-load conditions with dc-link voltage balancing controller activated (switching frequency = 1 kHz): Channel 1: V_{dc1} (100V/div), Channel 2: V_{dc2} (100V/div), Channel 3: phase-*a*1 current (1A/div), Channel 4: speed (500rpm/div), Horizontal: Time (400ms/div). (Markers for Channels 1 and 2 are overlapped).

D.Simulations in Generating Mode

By comparing the experimental and simulation results presented in sub-section V-A, it can be concluded that the Matlab/Simulink simulator gives an accurate representation of the actual system. Here, investigations using the same simulator are presented to verify the operation of the system in generating mode. In the simulation, the total dc-link voltage is maintained at 600 V and the generator is subjected to a varying wind speed profile, shown in Fig. 27. All simulation results are shown from t = 2.0 s onwards, when the machine has reached a steady-state operating point at rated wind speed.

An additional resistance R = 2.8 Ω is added again in phases *a*1*b*1*c*1 to emulate the winding asymmetry. Fig. 28 shows the unbalanced dc-link voltage when the generator is controlled using only *d-q* current controllers, with no dc-link voltage balancing control. The phase currents under this operating condition are unbalanced, with current amplitudes in winding 1 lower than those in winding 2 (Fig. 29). This is the result of

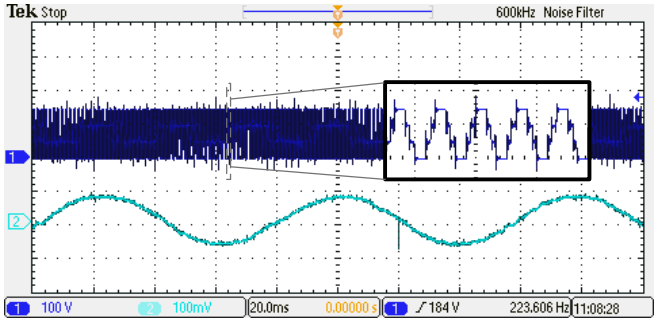

Fig. 25. Experimental results for the machine running at 250rpm without load with dc-link voltage balancing controller activated: Channel 1: CMV for winding 1 (100V/div), Channel 2: phase-*a*1 current (1A/div).

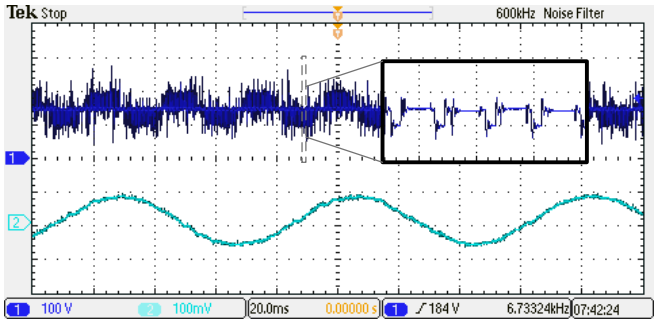

Fig. 26. Experimental results for the machine running at 250rpm without load with dc-link voltage balancing controller activated: Channel 1: Neutral-to-neutral voltage (100V/div), Channel 2: phase-*a*1 current (1A/div).

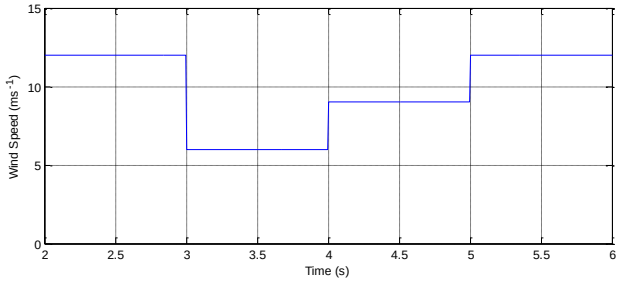

Fig. 27. Wind speed variation used for simulating the system in generating mode of operation.

the non-zero *x-y* currents that, according to (21), lead to the current asymmetry. Since the voltage drift in this case is not severe enough to saturate the VSCs, the distortions in phase currents are less significant. Remaining distortion is caused by the uncontrolled *x-y* currents and the uncompensated dead-time effect.

The same test is then repeated but with the dc-link voltage balancing controller activated. Fig. 30 shows that the dc-link voltages are now balanced and are kept at the equal level. The phase currents in Fig. 31 still show different amplitudes but now the currents in winding 1 are higher than those in the winding 2. This is so because, in order to achieve dc-link voltage balancing, more active power needs to be generated in winding 1 to compensate for the larger copper loss due to the additional resistance *R*. Even though the dc-link voltage balancing controller injects non-zero steady-state *x-y* currents, the amount of these circulating currents is lower than those in the previous case (with uncontrolled *x-y* currents) and this reduces the current waveform distortion. The injection of these steady-state *x-y* currents, caused by the generator asymmetries, produces additional stator winding losses. Fig. 32 shows the *d-q* currents under the varying wind speed conditions. Flux current is maintained at a constant level, while torque current is varied to follow the MPPT operation.

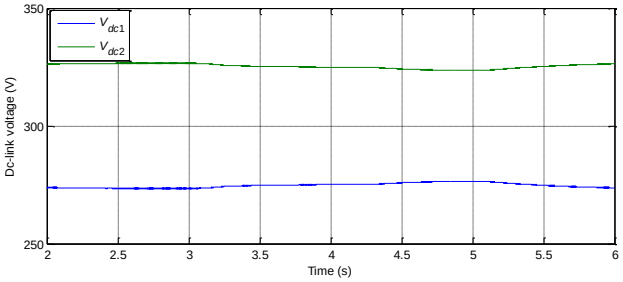

Fig. 28. Dc-link voltages under varying wind speed, with no dc-link voltage balancing controller.

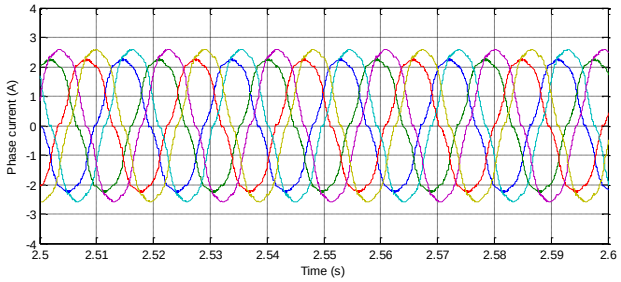

Fig. 29. Phase currents for generating operation without dc-link voltage balancing controller.

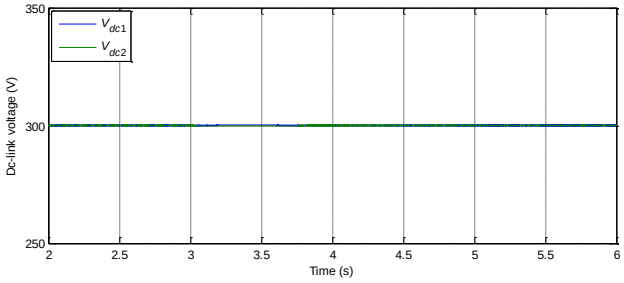

Fig. 30. Dc-link voltages under varying wind speed, with dc-link voltage balancing controller (V_{dc1} and V_{dc2} are overlapped).

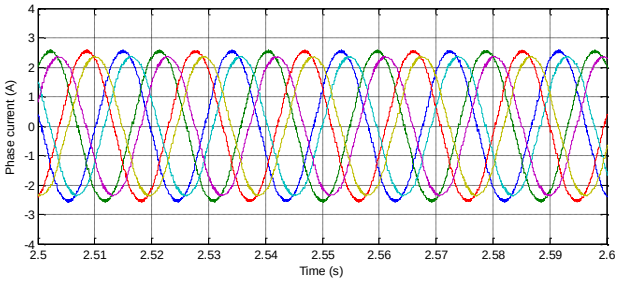

Fig. 31. Phase currents for generating operation with dc-link voltage balancing controller.

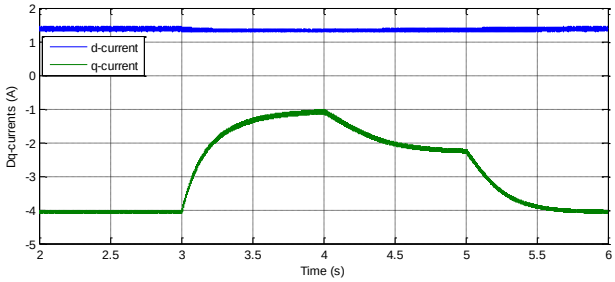

Fig. 32. *D-q* currents for generating operation with dc-link voltage balancing controller.

The flux and torque operation of the generator is practically unaffected by the dc-link voltage balancing controller. The simulation results for the generating mode show that, with the dc-link voltage balancing controller, the generator is able to operate with proper flux and torque control.

VI. Conclusion

This paper discusses the viability of an asymmetrical six-phase energy conversion system with cascaded machine-side converters and presents a method for the voltage balancing of the dc-link midpoint. The topology and the concept are equally applicable to both variable-speed drive and generation applications.

The series connection of the converters halves the individual dc-link voltages and the common-mode voltage's *dv/dt*. However, the voltage shifting between the two isolated neutral points can prevent the use of low voltage machines unless specific PWM techniques are employed. The system is believed to be well-suited to remote offshore wind farms with HVDC connection, where elevation of the dc-link voltage and the use of only two cables for the grid-side connection can reduce the overall infrastructure cost, but there is a potential problem with the drift of the dc-link midpoint voltage. This work overcomes this limitation by developing a dc-link voltage balancing controller that uses the *x-y* currents to unbalance the winding currents in order to balance the power sharing between the two sets of three-phase windings. This represents an entirely new way of exploiting the existence of additional degrees of freedom, available in multiphase machines, which has never been reported before. Simulation and experimental results confirm that it is possible to accurately control the dc-link midpoint voltage and to operate the machine in variable-speed mode in both motoring and generation.

REFERENCES

[1] H. Abu-Rub, J. Holtz, J. Rodriguez, and G. Baoming, "Medium-voltage multilevel converters - state of the art, challenges, and requirements in industrial applications," *IEEE Trans. on Ind. Electr.*, vol. 57, no. 8, pp. 2581–2596, 2010.

[2] S. Kouro, J. Rodriguez, B. Wu, S. Bernet, and M. Perez, "Powering the future of industry: High-power adjustable speed drive topologies," *IEEE Ind. Appl. Magazine*, vol. 18, no. 4, pp. 26–39, 2012.

[3] E. Levi, R. Bojoi, F. Profumo, H. A. Toliyat, and S. Williamson, "Multiphase induction motor drives – a technology status review," *IET Electric Power Applications*, vol. 1, no. 4, pp. 489-516, 2007.

[4] N. E. A. M. Hassanain and J. E. Fletcher, "Steady-state performance assessment of three- and five-phase permanent magnet generators connected to a diode bridge rectifier under open-circuit faults," *IET Renewable Power Generation*, vol. 4, no. 5, pp. 420-427, 2010.

[5] M. J. Duran, S. Kouro, B. Wu, E. Levi, F. Barrero, and S. Alepuz, "Six-phase PMSG wind energy conversion system based on medium-voltage multilevel converter," in *Proc. Eur. Conf. on Power Electr. and Applications EPE*, CD-ROM, 2011.

[6] G. K. Singh, A. Senthil Kumar, and R. P. Saini, "Selection of capacitance for self-excited six-phase induction generator for stand-alone renewable energy generation," *Energy*, vol. 35, no. 8, pp. 3273-3283, 2010.

[7] X. Li and O. P. Malik, "Performance of a double-star synchronous generator with bridge rectified output," *IEEE Trans. on Energy Conv.*, vol. 9, no. 3, pp. 613-619, 1994.

[8] X. Yuan, J. Chai, and Y. Li, "A transformer-less high-power converter for large permanent magnet wind generator systems," *IEEE Trans. on Sustainable Energy*, vol. 3, no. 3, pp. 318–329, 2012.

[9] F. Bu, W. Huang, Y. Hu, and K. Shi, "An integrated AC and DC hybrid generation system using dual-stator-winding induction generator with static excitation controller," *IEEE Trans. on Energy Conv.*, vol. 27, no. 3, pp. 810–812, 2012.

[10] F. Bu, W. Huang, Y. Hu, J. Shi, and K. Shi, "A stand-alone dual stator-winding induction generator variable frequency AC power system," *IEEE Trans. on Power Electr.*, vol. 27, no. 1, pp. 10–13, 2012.

[11] S. Brisset, D. Vizireanu, and P. Brochet, "Design and optimization of a nine-phase axial-flux PM synchronous generator with concentrated winding for direct-drive wind turbine," *IEEE Trans. on Ind. Appl.*, vol. 44, no. 3, pp. 707-715, 2008.

[12] A. Di Gerlando, G. Foglia, M. F. Iacchetti, and R. Perini, "Analysis and test of diode rectifier solutions in grid-connected wind energy conversion systems employing modular permanent-magnet synchronous generators," *IEEE Trans. on Ind. Electr.*, vol. 59, no. 5, pp. 2135–2146, 2012.

[13] Z. Zhang, Y. Yan, S. Yang, and Z. Bo, "Development of a new permanent-magnet BLDC generator using 12-phase half-wave rectifier," *IEEE Trans. on Ind. Electr.*, vol. 56, no. 6, pp. 2023-2029, 2009.

[14] Z. Xiang-Jun, Y. Yongbing, Z. Hongtao, L. Ying, F. Luguang, and Y. Xu, "Modelling and control of a multi-phase permanent magnet synchronous generator and efficient hybrid 3L-converters for large direct-drive wind turbines," *IET Electric Power Applications*, vol. 6, no. 6, pp. 322–331, 2012.

[15] B. Andresen and J. Birk, "A high power density converter system for the Gamesa G10x 4,5 MW wind turbine," in *Proc. European Conf. on Power Electr. and Applications EPE*, CD-ROM, 2007.

[16] H.S. Che, M.J. Duran, W.P. Hew, N.A. Rahim, E. Levi, and M. Jones, "Dc-link voltage balancing of six-phase wind energy systems with series-connected machine-side converters and NPC grid-side converter," in *IEEE Annual Conf. of Ind. Electr. Society IECON*, 2012, pp. 3541–3546.

[17] M. Liserre, R. Cárdenas, M. Molinas, and J. Rodríguez, "Overview of multi-MW wind turbines and wind parks," *IEEE Trans. on Ind. Electr.*, vol. 58, no. 4, pp. 1081–1095, 2011.

[18] X. Sun, D. Huang, and G. Wu, "The current state of offshore wind energy technology development," *Energy*, vol. 41, no. 1, pp. 298–312, May 2012.

[19] B. Wu, Y. Lang, N. Zargari, and S. Kouro, "*Power conversion and control of wind energy systems*," IEEE Press - John Wiley and Sons, Hoboken, NJ, 2011.

[20] H.S. Che, W.P. Hew, N.A. Rahim, E. Levi, M. Jones, and M.J. Duran, "A six-phase wind energy induction generator system with series-connected DC-links," in *Proc. IEEE Power Electr. for Distributed Generation Systems PEDG*, pp. 26-33, 2012.

[21] M. A. Parker, C. Ng, and L. Ran, "Fault-tolerant control for a modular generator–converter scheme for direct-drive wind turbines," *IEEE Trans. on Ind. Electr.*, vol. 58, no. 1, pp. 305-315, 2011.

[22] C. H. Ng, M. A. Parker, L. Ran, P. J. Tavner, J. R. Bumby, and E. Spooner, "A multilevel modular converter for a large, light weight wind turbine generator," *IEEE Trans. on Power Electr.*, vol. 23, no. 3, pp. 1062-1074, 2008.

[23] P. K. Olsen, S. Gjerde, R. M. Nilssen, J. Hoelto, and S. Hvidsten, "A transformerless generator-converter concept making feasible a 100 kV light weight offshore wind turbine: part I - The generator," in *IEEE Energy Conv. Congress and Exposition ECCE*, 2012, pp. 247–252.

[24] S. S. Gjerde, P. K. Olsen, and T. M. Undeland, "A transformerless generator-converter concept making feasible a 100 kV low weight offshore wind turbine part II - The converter," in *IEEE Energy Conv. Congress and Exposition ECCE*, 2012, pp. 253–260.

[25] S. S. Gjerde and T. M. Undeland, "A modular series connected converter for a 10 MW, 36 kV, transformer-less offshore wind power generator drive," *Energy Procedia*, vol. 24, no. January, pp. 68–75, Jan. 2012.

[26] M. A. Parker, L. Ran, and S. J. Finney, "Distributed control of a fault-tolerant modular inverter for direct-drive wind turbine grid interfacing," *IEEE Trans. on Ind. Electr.*, vol. 60, no. 2, pp. 509–522, 2013.

[27] R. Bojoi, E. Levi, F. Farina, A. Tenconi, and F. Profumo, "Dual three-phase induction motor drive with digital current control in the stationary reference frame," *IEE Proceedings - Electric Power Application*, vol. 153, no. 1, pp. 129-139, 2006.

[28] M. Jones, S. N. Vukosavic, D. Dujic, and E. Levi, "A synchronous current control scheme for multiphase induction motor drives," *IEEE Trans. on Energy Conv.*, vol. 24, no. 4, pp. 860-868, 2009.

[29] K. Marouani, L. Baghli, D. Hadiouche, A. Kheloui, and A. Rezzoug, "A new PWM strategy based on a 24-sector vector space decomposition for a six-phase VSI-fed dual stator induction motor," *IEEE Trans. on Ind. Electr.*, vol. 55, no. 5, pp. 1910-1920, 2008.

[30] R. Bojoi, A. Tenconi, F. Profumo, G. Griva, and D. Martinello, "Complete analysis and comparative study of digital modulation techniques for dual three-phase AC motor drives," in *Proc. IEEE Power Electr. Spec. Conf. PESC*, pp. 851-857, 2002.

[31] M. J. Duran, J. Prieto, F. Barrero, J. A. Riveros, and H. Guzman, "Space vector PWM with reduced common–mode voltage for five–phase induction motor drives," *IEEE Trans. on Ind. Electr.*, 2013 (d.o.i: 10.1109/TIE.2012.2217719).

Hang Seng Che received his BEng degree in Electrical Engineering from the University of Malaya, Kuala Lumpur, Malaysia, in 2009. He is a recipient of the Kuok Foundation Postgraduate Scholarship Award for his PhD study, and is currently working towards his PhD degree under auspices of a dual PhD programme between the University of Malaya and Liverpool John Moores University. His research interests include multiphase machines and renewable energy.

Emil Levi (S'89, M'92, SM'99, F'09) received his M.Sc. and PhD degrees from the University of Belgrade, Yugoslavia in 1986 and 1990, respectively. From 1982 till 1992 he was with the Dept. of Elec. Engineering, University of Novi Sad. He joined Liverpool John Moores University, UK in May 1992 and is since September 2000 Professor of Electric Machines and Drives. He serves as Co-Editor-in-Chief of the IEEE Trans. on Industrial Electronics, as an Editor of the IEEE Trans. on Energy Conversion, and as Editor-in-Chief of the IET Electric Power Applications. Emil is the recipient of the Cyril Veinott award of the IEEE Power and Energy Society for 2009.

Martin Jones received his BEng degree (First Class Honours) in Electrical Engineering from the Liverpool John Moores University, UK in 2001. He was a research student at the Liverpool John Moores University from September 2001 till Spring 2005, when he received his PhD degree. Dr Jones was a recipient of the IEE Robinson Research Scholarship for his PhD studies and is currently with Liverpool John Moores University as a Reader. His research is in the area of high performance ac drives.

Mario J. Duran was born in Málaga, Spain, in 1975. He received the M.Sc. and PhD degrees in Electrical Engineering from the University of Málaga, Spain, in 1999 and 2003, respectively. He is currently an Associate Professor with the Department of Electrical Engineering at the University of Málaga. His research interests include modeling and control of multiphase drives and renewable energies conversion systems.

Wooi-Ping Hew obtained his BEng and Masters (Electrical) degrees from the University of Technology, Malaysia. He received his PhD from the University of Malaya, Kuala Lumpur, Malaysia in 2000. He is currently a Professor in the Faculty of Engineering, University of Malaya, Kuala Lumpur, Malaysia. Dr. Hew is a Member of IET and a Chartered Engineer. His research interests include electrical drives and electrical machine design.

Nasrudin A. Rahim (M'89–SM'08) received the B.Sc. (Hons.) and M.Sc. degrees from the University of Strathclyde, Glasgow, U.K., and the PhD degree from Heriot–Watt University, Edinburgh, U.K., in 1995. He is currently a Professor with the Faculty of Engineering, University of Malaya, Kuala Lumpur, Malaysia, where he is also the Director of the Power Energy Dedicated Advanced Center (UMPEDAC). Prof. Rahim is a Fellow of the IET, U.K., and the Academy of Sciences Malaysia.